In-situ observation of radiation physics and chemistry of nanostructured cerium oxide in water

Muhammad Sajid Ali Asghar[1], Beverley Inkson[1], Sudipta Seal[2], Marco Molinari[3], Dean Sayle[4] and Günter Möbus[1]

[1] NanoLAB Centre, Department of Materials Science and Engineering, The University of Sheffield, Sheffield S1 3JD, United Kingdom

[2] Advanced Materials Processing Analysis Center (AMPAC) and Nanoscience Technology Center (NSTC), Material Science and Engineering, College of Medicine, University of Central Florida, Florida 32816, United States of America

[3] Department of Chemical Sciences, University of Huddersfield, Queensgate, Huddersfield, HD1 3DH, United Kingdom

[4] School of Physical Sciences, University of Kent, Canterbury CT2 7NZ, United Kingdom

E-mail: g.moebus@sheffield.ac.uk

Keywords: electron irradiation, radiolysis, ceria nanoparticles, in-situ TEM, liquid cell TEM

Abstract

Room temperature electron irradiation in aqueous environment is applied to CeO_2 nanoparticles using a transmission electron microscope equipped with liquid environmental cell. Oxide dissolution kinetics become accessible at unprecedented scale of spatial and time resolution through irradiation activation of water within a sub-μm size volume, allowing direct measurements of transformation rate and morphologies. Successful live-observation of the formation of nano-needles provides essential inside in how 1D-nanostructures can form. Furthermore, formation of hydrogen bubbles is found and interpreted in relation to the dose needed for ceria dissolution. The results are of importance for many research applications of ceria in water, e.g. for catalysis, environmental remediation, biomedical radiation protection, anti-corrosion coatings, and ultimately via analogy to UO_2 also for fission-power fuel engineering and waste disposal.

1. Introduction

Ceria Nanoparticles (CNPs) are one of the most remarkable and versatile multi-functional nanomaterials with wide-ranging applications from catalysis over optical and biomedical fields to machining [1]. Typically, characterisation studies on the nanoscale, such as TEM of dry powders, aim at the defect structure, distribution of oxygen vacancies, and the ionic mobility in bulk and at the surface. However, the majority of applications of CNPs use aqueous environment, and therefore nano-characterisation would be incomplete unless the CNP-water interaction, including possible corrosion behaviour, is studied in situ. Prominent uses of CNPs in water include e.g. abrasive materials for the polishing of glasses and for chemical-mechanical planarization of electronic integrated circuit materials [2], sun screens to protect from ultraviolet rays [3], anti-corrosion coatings on metals [4], diesel fuel additives for a more complete combustion to abate soot formation [5], environmental cleaning and remediation [6] and for various concepts in catalysis [7]. More recently, the antioxidant [8], and radio-protection properties of CNPs in cellular liquid environment have been explored, aiming e.g. at neuro protection [9] or improved cancer treatment [10, 11]. Additionally, ceria is a common non-radioactive analogue for UO_2 and ThO_2, for which irradiation and dissolution are major study subjects in nuclear fuel specification during operation as well as for spent fuel disposal [12]. For the latter three applications (environmental remediation, biomedical protection, and nuclear ceria) a common feature is the combined application of ceria in water under external radiation. While ceria material is known to be exceptionally stable with respect to both reactive chemical and irradiative [13, 14] environments, no studies seem to specialise on combined irradiation chemical reaction and corrosion. The advent of liquid cell TEM [15, 16] has opened up the capability to study samples involving an electron transparent thin film of liquid giving valuable results in NP-growth [17], NP-movements [18, 19], and occasionally nanoparticle shrinkage [20].

Ceria reactions with water molecules are typically studied as part of catalytic reactors or fuel cells [21–23] emphasising water splitting but ignoring reverse effects of the water-split products on ceria surface and the integrity of the fluorite structure. Acid dissolution of ceria on the other hand is an ongoing bulk-chemistry research topic [14, 24]. However, in any published data the dissolution rate of ceria remains rather small even under modified experimental conditions including ultrasound [24], addition of Pt catalyst particles, or using multiple acids [14]. A detailed study of ex situ irradiative ceria dissolution in water from a nuclear materials point of view [25] finds evidence of radiation-induced acceleration of dissolution. Solubility of cerium phases and dissolved ionic species have been discussed as function of pH [26, 27], based on earlier work [28–30]. Here we use liquid cell TEM for a first comprehensive and dedicated study of the multi-stage corrosion behaviour of nanostructured CeO_2 in water under radiolytic conditions. In expansion of our recent work [31], we use the electron beam induced activation of water as a deliberate ultra-fast accelerated testing tool for qualitative and quantitative studies of ceria dissolution. Here we accompany dissolution studies with in situ live observation of secondary effects, including formation of secondary phases, and generation of gas bubble.

2. Method

Ceria nanoparticulate powders are sampled from pre-manufactured nanoparticle dispersions for liquid cell TEM observation, followed by specific in situ electron irradiation procedures. Particles are either 10–40 nm size commercial ceria nanoparticles (CeO_2, purity >99.9%), characterised earlier [32], or ceria nanorods fabricated as described earlier [33, 34].

Ceria nano-particles are suspended in DI water to be placed into the liquid cell (model Protochips Poseidon P500 [35]) comprising a microfluidic cell of two Si_3N_4 membranes. Samples are directly loaded as aqueous suspensions onto the chip, while after insertion into the TEM we occasionally injected further small quantities of water via a syringe into the cell, whenever needed to mobilise particles. For imaging and digital video recording we mainly use a JEOL JEM 3010 TEM operated at 300 kV, while a JEOL JEM 2010-F, operated at 200 kV, is used where mentioned.

The electron irradiation in both electron microscopes is applied with largest condenser aperture (CA) and spot size 1. At normal imaging intensity at 300 kV (roughly below ≈1 nA μm^{-2}), extended observations of movement of nanoparticles can be achieved with little dissolution. However, above an intensity range of ≈3 nA μm^{-2}, ceria is found to chemically react with irradiated water (detailed values depend on water thickness), and it is this 2nd regime which is the topic of this paper. All experiments dealing with particle dissolution had the electron beam spread onto an area of at least 2 μm diameter. Further converging of the beam to below 2 μm has been realised for figure 5 to increase the intensity range seven-fold, exclusively for the purpose of triggering gas bubble formation.

3. Results

The multiple in situ electron irradiation experiments reported here are detailed in order of consecutive observation of effects, starting with 'Stage 1' comprising all particle corrosion or dissolution effects, followed by 'Stage 2' comprising observation of new solid phases, and finally 'Stage 3' including gas bubble formation.

3.1. Stage 1: corrosion of nanoscale cerium oxide of particle and rod shape

The primary observation (stage 1) of electron irradiation of CNPs in water shows corrosion attack localised to the irradiation volume, with eventual complete dissolution. Here we concentrate on studying the influence of particle type (nanorod, nanosphere), irradiation voltage, and irradiation intensity. In-situ imaging is also used to track the complex kinetic behaviour of the corrosion process. Rather than being confined to volume loss per time interval, the process of corrosion comprises specific particle shape changes, ranging from particle rounding to roughening and changes of aspect ratio, but also changing particle attachment geometries.

Due to the wide-spread interest in oxide-corrosion at room temperature, it is our aim not only to capture dissolution behaviour on video sequences, but also to quantify and compare with previously reported, laboratory wet-chemistry based, dissolution rates.

Extended low-intensity imaging of nanoparticle agglomerates is possible in liquid cell TEM, e.g. for selecting regions of interest and for focusing, by keeping beam intensity below a threshold or critical intensity. If the threshold is exceeded, dissolution is triggered immediately, figures 1(a)–(c). The sequence demonstrates, that for sufficient irradiation ultimately dissolution is completely achieved irrespective of the starting shape and starting size of nanoparticles and that at the end of stage 1, ionically enriched water resulting from fully dissolved particles temporarily persists. A potentially important aspect of the dissolution experiments is the amount of convection between irradiated and non-irradiated water: figures 1(d)–(e) show in situ imaging of a completed local irradiation and dissolution experiment. Here, in figure 1(d) the sample has been swiftly moved laterally to allow comparison of irradiated (bottom right, CNPs dissolved) and non-irradiated sample (top left, full CNP density). In the other image, figure 1(e), sudden magnification reduction achieves the same purpose. Essentially, a sharp borderline outlining the original beam-contour confirms that the spatial concentration profile between highly reactive ionised water (inside) and original DI water (outside) is retained, and convective blurring can temporarily be kept small (the non-round apparent beam-shape in 1e might be due to some convection effect).

From the volume-loss V per image interval t, normalised to the particle surface-area A at the start of t, and the material density ρ, corrosion rates R are calculated by equation (1):

$$R = \rho \Delta V / A \Delta t \qquad (1)$$

The dissolution rates are approximate by assuming symmetry of revolution (volumes are estimated from projections), and also vary from particle to particle, depending on thickness of water-layer, local electron intensity, and contact of particle to the silicon nitride membranes of the liquid cell as well as to other particles. Time intervalls printed onto figures 1–3 do not indicate the start of the irradiation, but the start of measurement, chosen after some pre-irradiation, once particles are clear enough to be tracked in isolation.

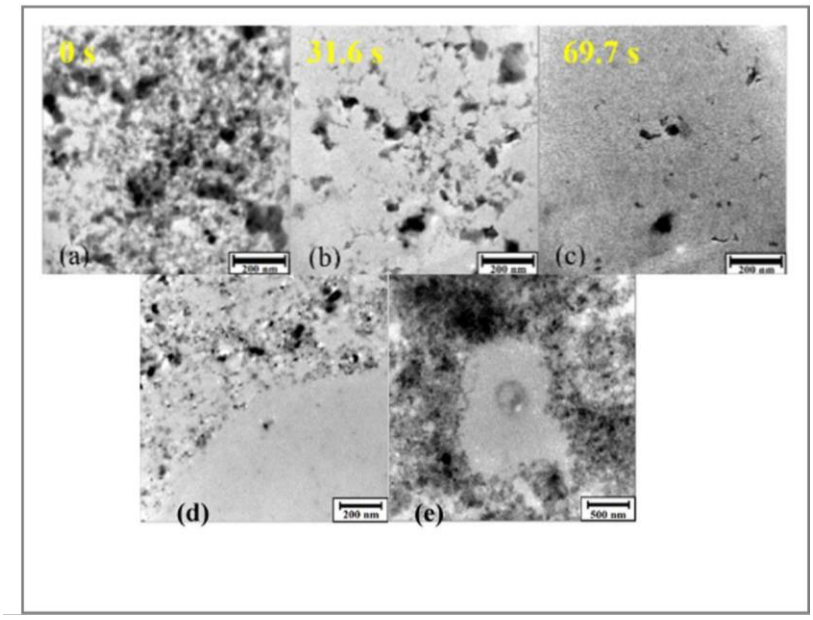

Figure 1. (a)–(c) Aqueous dissolution of ceria nanoparticle powder during electron irradiation; (d), (e) Comparison of sample before and after irradiation-dissolution: beam shift (d) and magnification-reduction (e) illustrating sharp circular borderline between the regions inside (no particles) and outside (original particles) the irradiation zone.

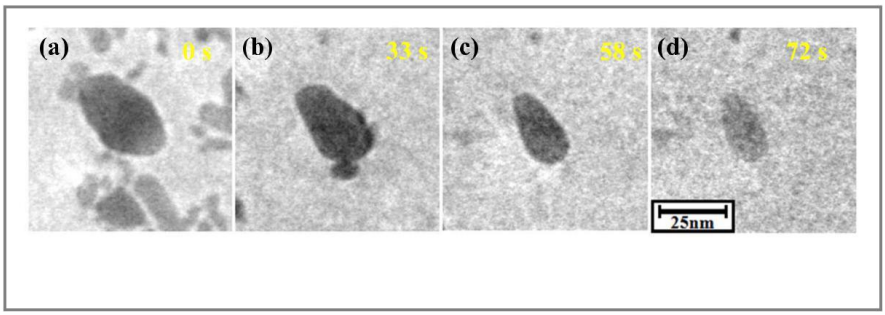

Figure 2. Sequence of ceria dissolution: (a)–(d) ceria nanoparticle involving particle aspect ratio increase before complete dissolution; (JEM 3010 at 300 kV).

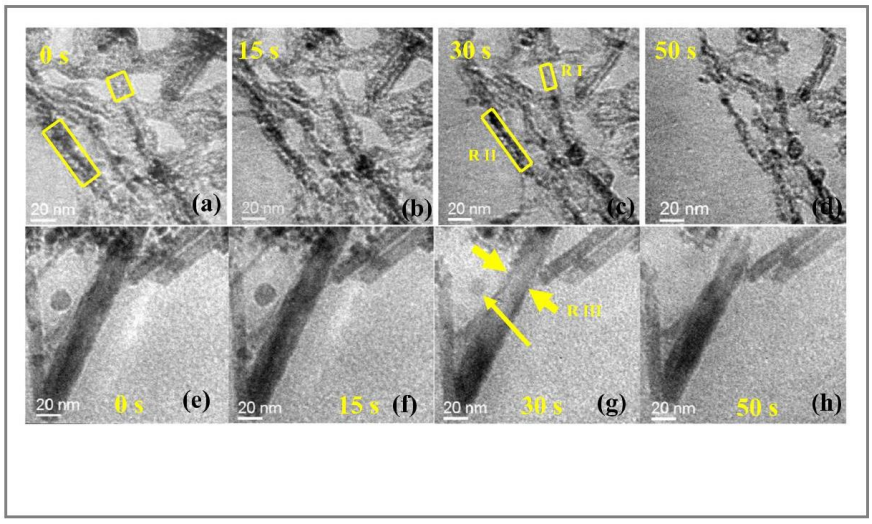

Figure 3. Dissolution of ceria nanorods (a)–(d) involving rough surface (JEM 2010-F at 200 kV; boxes indicate measured items for table 1). (e)–(h) dissolution of straight, smooth and homogeneous ceria nanorod along with one round nanoparticle (JEM-2010-F at 200 kV; arrows indicate measured items for table 1).

Table 1 Quantified ceria dissolution rates of nanoparticles and nanorods in comparison with earlier work.

S. no	Object	R_{min} (g/m^2/day) (SE)	R_{max} (g/m^2/day) (SE)
[31]	CNPs, 300 kV: sphere, oval and octahedral	7	700
1	Rod I 200 kV	25(±0.8)	99(±0.3)
2	Rod II 200 kV	30(±1)	83(±2)
3	Rod III 200 kV	06(±2)	13(±6)
4	Sphere NP 200 kV	35(±3)	192(±19)

In extension of the preliminary measurements in [31], corrosion of some non-spherical CNPs are now detailed in figure 2. This figure also serves to highlight some challenge to quantification, as during overall shrinkage of particles lateral movement, rotation in 3D, and shape changes occur. Figures 2(a)–(d) is an oval shaped object. We observe that sharp corners and annexed rough features are disappearing first by rounding, however the rounding is not progressing monotonously. Tracking of aspect ratio reveals that ratios can increase from 1.6 to 2.1, figures 2(a)–(d). The shape change is therefore now found more complex than simple minimisation of surface energy resulting in spheres found earlier [31].

Due to the complex dissolution found for CNPs of various roundness, it is of interest to compare nanoparticles with ceria nanorods (CNRs) as dissolution targets, see figure 3. CNRs are suggested to result from needle-shape hydroxide nucleation events during ex situ synthesis before transforming to ceria during hydrothermal ageing [33, 34]. With the cylindrical symmetry pre-existing, volume losses can be quantified easily from a suitably chosen cylindrical segment. We observe two sets of nanorods, one sample (figures 3(a)–(d)) contains nanorods with visible imperfections in straightness, flatness of surface, and being internally inhomogenous. The other sample (figures 3(e)–(h)) shows smooth and flat nanorods. At the same time a spurious CNP is found next to the smooth rods as a minority phase, which provides important calibration.

Dissolution data for ceria nano-objects (particles and rods) are collected in table 1, with items 1–4 referring to objects of figures 3(a)–(d) and (e)–(h). For each object dissolution rates are found to vary over time and the indicated range refers to a lower and upper limit for early (slow) and late (faster) dissolution. Each data is the average of multiple diameter measurements, reported as standard error (SE), units of $gm^{-2}day^{-1}$ are preferred to facilitate comparison with literature.

Comparing the dissolution rates for the two types of nanorods, we find that the average data of the two rough nanorods (Rod I and II) is about 7 times faster than the data for the smooth CNR (Rod III), see table 1. This is expected as roughness in any corrosion process, provides an extra enhancement of active surface, not entered into the surface-estimates for the dissolution formula. On the other hand it is interesting to compare nanorods with nanoparticles, and here the data for the rough nanorods are found to be within the range of our various findings for nanoparticles. However, the smooth CNR (table 1, item 3) shows an order of magnitude slower shrinkage than most nanoparticles. It appears that the higher surface curvature of particles relative to rods accelerates dissolution in the same way as roughening of the rods. Finally, the influence of voltage is examined: while the nanoparticle samples (figures 1 and 2) are examined at 300 keV, this latter CNP (table 1, item 4) on the nanorod sample, examined at 200 keV, gives important evidence of the influence of beam energy on dissolution rate, which is found to be limited to only within one order of magnitude, comparing item 4 with item 0 (row 1) of table 1.

In summary, the dissolution rates for nanorods, elongated nanoparticles and round nanoparticles were of similar order of magnitude of data, confirming a robustness of the measurement across various experiments, with unavoidable variation in water-thickness, which influences irradiation effects.

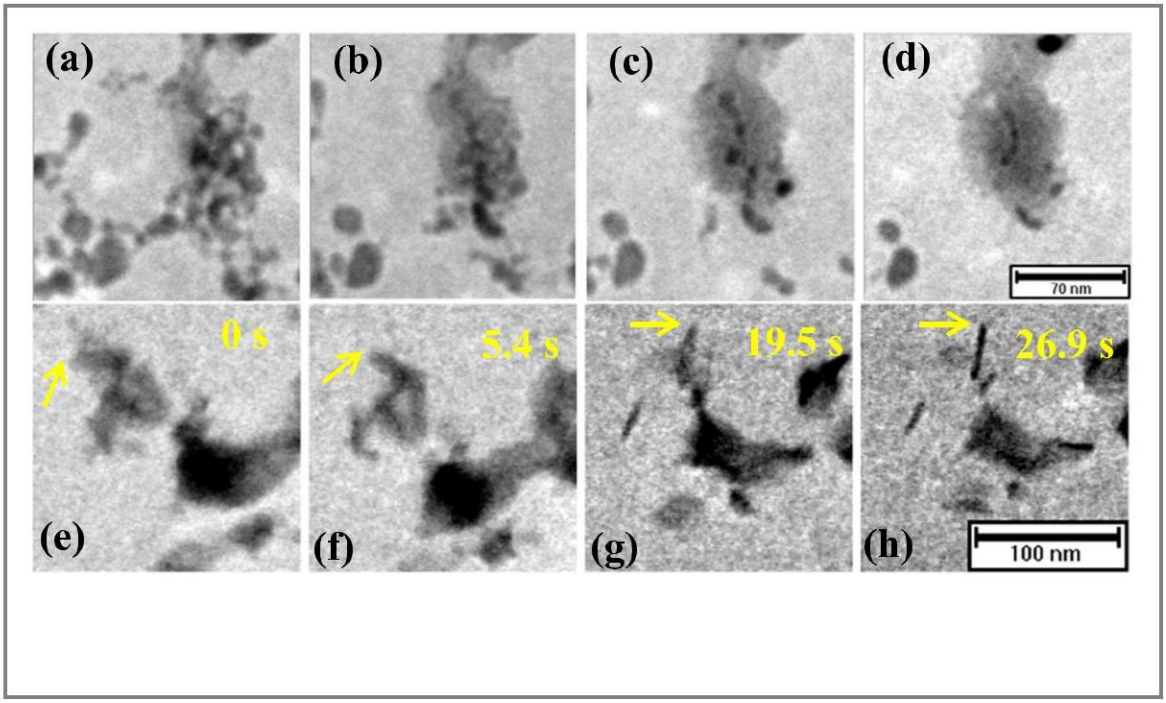

Figure 4. Parallel formation and dissolution: (a)–(d) Growth of amorphous phase around and replacing raw nanoparticles. (e)–(h) Transformation of 3D irregular shaped particles into needle shaped particles. The arrow helps tracking one corner of a particle rotating while transforming.

3.2. Stage 2: formation of new phases

The dissolution of nanoparticles leads to the water film becoming enriched in cerium ions and compound + more stable state once irradiation levels, local concentrations or pH change significantly. It can be expected that some new solid phases form. Live electron diffraction recording confirms that all initial fluorite ceria Bragg reflections disappear *in situ* and electron scattering from residual material along with water and amorphous Si_3N_4 membranes contributes to the halo-features seen in the final-state diffraction. However, small volumes of new crystalline minority phases, not visibly contributing to a wide area diffraction pattern, are nevertheless expected to persist.
The main distinction in newly formed phases is the mass-thickness and Bragg scattering contrasts:

On the one hand, several distinct lightly scattering phases (low average atomic number) one of which is illustrated in figures 4(a)–(d). These phases exceed the original particles in size and sometimes surround the latter or link them into chains, or replace them over time.

On the other hand, we find new dark (high atomic number), strongly scattering phases, which can be further subdivided into 1D structures of predominantly needle shape (figures 4(g)–(h)) and predominantly roundish particles (figure 5) which exceed the size of the raw ceria nanoparticles, and which do not show any octahedral morphology.

The main difference of above dark and bright phases is the occurence of Bragg scattering features: these are either displaced white spots (shadow images of dark particles) or contours inside dark particles, both requiring lattice planes. Therefore all dark particles in figures 4(a)–(h) are identified as crystalline. In contrast, the bright phase of figures 4(a)–(d) never shows such Bragg features, and also has a non-facetted morphological appearance, both indicating an amorphous phase.

While the dark phases suffer eventual dissolution similar to the original particles, the amorphous phases appear stable against beam-induced dissolution. The needles appear to be a transient phase, forming at rather late stage during raw particle dissolution, before being finally subjected to dissolution themselves. For both figures 4 and 5, the time calibration is relative to a chosen start, the image labelled '0 s' would already had experienced some time of irradiation.

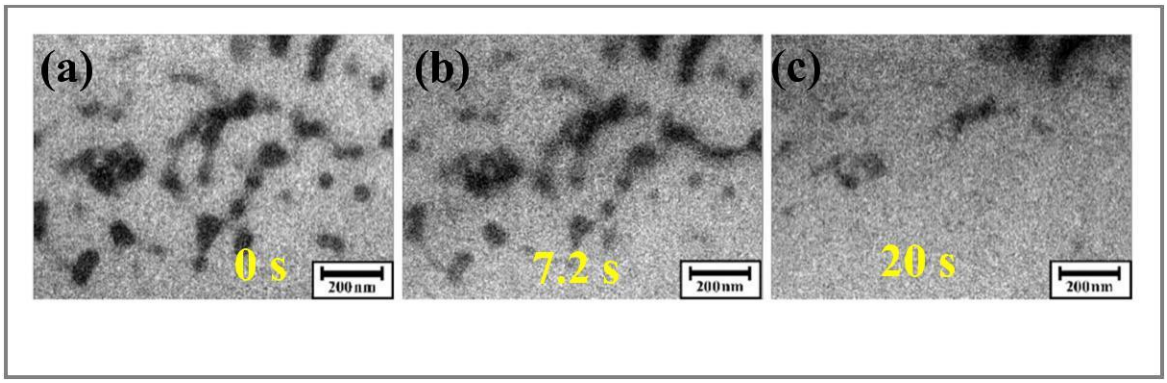

Figure 5. Roundish dark contrast particles of >50 nm size, dissolving eventually under irradiation (scale bar of 200 nm).

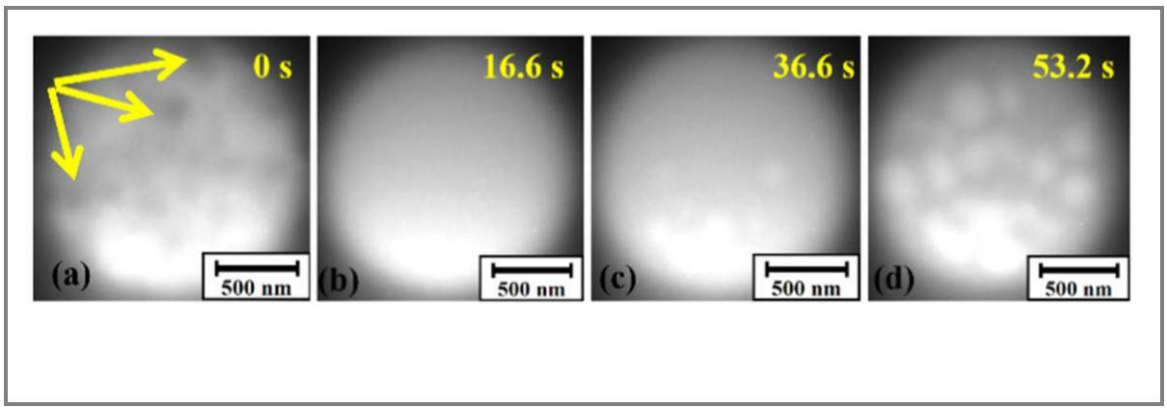

Figure 6. Nano bubble formation and their growth at very high intensity of electron beam irradiation with (a) yellow arrows showing residual nanoparticles, (b) complete dissolution of CNPs, (c) bubble formation and (d) growth of bubbles.

3.3. Stage 3: gas bubble formation

Using the highest achievable intensity irradiation (see methods), the timing and relationship of CNP dissolution and gas bubble generation is explored. In figure 6 four stages of radiolytic behaviour are compared, all at identical intensity (seven-fold higher than in dissolution experiments above). In figure 6(a) the initial presence of the last few ceria NPs can still be seen (arrows), while in figure 6(b) all particles have vanished due to progressive dissolution. Continued irradiation for figure 6(c) then kick-starts the formation of nano-bubbles in water, indicated as bright spherical features. The size and number of bubbles continues to increase to over 150 nm diameter (figure 6(d)). Following earlier observations in the literature [36] they are most likely due to the formation of molecular hydrogen within the irradiated water volume in the liquid cell. The phenomenon of formation of bubbles when water is irradiated by electron beams of >100 kV is well known [36]. Here we aim to put the effect into context relative to ceria dissolution, finding that the irradiation dose necessary to generate bubbles is significantly higher than for ceria NP dissolution.

4. Discussion

The three stages of response of our water-particle-system to irradiation are discussed with respect to the modifications to water imposed by the electron beam. Dissolution studies of materials by liquid cell TEM are rare and mostly reported as side effect of particle growth studies [37, 38], such as calcium carbonate and Au NPs [15, 39], etching of Pd NPs [20], and ZnO NPs [40]. The radiolysis of water caused by the electron beam is known to change pH, and artificial acidity down to pH = 3 has been modelled [36] specifically for liquid cell TEM conditions starting with pure de-ionised water. Nano-ceria stability in water has been tuned by pH variation via induced surface charges as function of ageing time and temperature [41]. A recent ex situ study of solution chemistry [26] proposes Ce^{III} released from CeO_2 particles in water below pH = 4. Such reductive dissolution is much faster than Ce^{IV} release at higher pH [26], matching therefore our case of dissolution exceeding any previously reported rates. Macroscopically, ceria and related actinide-oxides in contact with water are known to either very slowly dissolve (environmental release studies [42]) or adopt a reaction layer (passivation layer, considered amorphous Me-hydroxide) on its surface (nuclear materials leaching studies [43]). Enhanced oxygen reactivity of wet ceria in comparison to dry ceria nanoparticles has been modelled by computer simulations [21, 44]. In agreement, ex situ laboratory-scale dissolution was found in thoria where the pH of solution was1.5–3 in 0.1 M NaCl [45]. Particle morphology influence is moderate, although sharp corners of irregular particles are primary dissolution locations complemented by locations with higher surface roughness or any features with excess of dangling bonds.

Dissolution (stage 1) and particle formation (stage 2) should be seen as overlapping stages in time, with the sequence of post-dissolution events to be explained via the Pourbaix E-pH diagrams for ceria from [29]: the water radiolysis experiment with its pH and redox changes therefore defines a trajectory in the Pourbaix diagram due to the formation of a variety of reactive species by water splitting [46, 47], equation (2):

$$H_2O \quad e^-_{aq},\ H^\bullet,\ OH^\bullet,\ HO_2^\bullet,\ OH^-,\ H_2,\ H_3O^+,\ H_2O_2 \qquad (2)$$

Here, e^-_{aq} denotes the hydrated electron and species marked ($^\bullet$) are radicals. The first two have a strong potential to chemically reduce ions in solution or on particle surfaces, while some others counteract as oxidiser [47]. Some products capable of oxide dissolution (e^-_{aq}, $H^\bullet$) are short lived and will be, during the time-scales of our dissolution experiment, complemented by longer lived products including the final two molecular species of equation (2) [36].

In agreement with [28–30], we point to the possibility of (metastable) hydroxide complexes forming possibly still in dispersion. There are two ways out of the metastable region (bottom left of Pourbaix diagram), either by upward-shift through oxidative precipitation [26, 27] leading to quaternary hydroxides, or through pH-reversal [48], leading to ternary hydroxides. Growth of solid or gel-type precipitates of $Ce(OH)_4 = CeO_2 \cdot 2H_2O$ appears possible in our case as follow-on after 'reductive dissolution' [27]. Equivalently, experiments on ThO_2 dissolution in the context of nuclear fission fuel rod dissolution [43] have found solid amorphous thorium-IV-hydroxide secondary products. However, unlike for Ce, Th has no ternary hydroxide option. Irradiation induced enhancement of the fraction of Ce^{3+} species in our CeO_2 particles is another mechanism, complementary to and distinct from standard reductive dissolution, where the Ce-reduction originates by water. Other most recent work have proposed alternatively either solid $Ce(OH)_3$ [48] species as end product or solid Ce_2O_3 species [49] as temporary intermediate. Our reported high dissolution rates [31] are however compatible with early stage persistance of CeO_2, and reproduced in [49].

Alternative concepts for new phases found in liquid-cell TEM experiments, discussed in the literature include: (i) carbon contamination [46] , mainly on the vacuum-side of the window; (ii) Formation of corrosive pitting layers have been found for calcium carbonate [39]. They are sharply bordered and of lower average atomic number, and associate more with core–shell appearances during dissolution, rather than with formation of new phases.

No report in any literature points to our unique needle phase as of figures 4(e)–(h). Its extreme anisotropy and dark contrast with sharp external facets, points to options of crystalline structure with unique axis: (i) Formation of hexagonal solid $Ce(OH)_3$, often evidenced via ex situ wet-chemical experiments [26, 33, 50], but unstable in air, is possible here as the liquid cell prevents air exposure. However, direct Ce^{III} to $Ce(OH)_3$ conversion is not favoured by Pourbaix analysis [27]. (ii) Relaxation of acidic pH back to near neutral could favour an elongated ceria crystal structure which achieves its 1D shape by oriented attachment [26, 50]. The latter option conforms with evidence of needles having same mass-thickness appearance as raw ceria particles. Unfortunately, no traces of this particular needle-phase could be found on any dry chips disassembled after the liquid cell experiment, supporting instability in air. Alternatively, growth of ternary Ce-hydroxide particles growing from a Ce-nitrate solution via pH-shift into highly alkaline regions have been explored in [48], however, achieving round particles, more like figure 5 here, instead of needles.

We discuss stage 3, the gas bubble formation, as part of our combined radiolysis experiment, as it is of central interest to associate the inferred hydrogen generation relative to ceria nanoparticle reactions, as there would be two pathways. (i) H formation by catalysis on ceria surfaces, or (ii) H formation by radiolysis of water alone (without CNPs involved). Figure 5 supports assumption (ii) necessitating a critical dose rate for enough hydrogen to be released simultaneously to react into stable molecular H_2 and start visible bubble formation. The absence of ceria NPs during later stages of bubble formation proves H_2 is not primarily resulting from a catalytic water-splitting effect known for water adsorbed to surfaces of ceria and zirconia [23, 47]. The latter might still happen in our case at minor rates, but its visibility is obscured by the dominant direct electron beam induced water splitting [47, 51].

5. Conclusions

Liquid cell TEM is successfully employed to observe in real-time a great variety of phenomena in the radiolytical dissolution and re-growth of cerium oxide and related nanostructures in a microfluid film of water. Apart from the innovative ability to video-record water-oxide reactions on nm-scale resolution with near TV rate time-resolution, some novel very specific findings are:

Nanorod formation is tracked in situ, transforming an isotropic nanomaterial into a 1D structure. Such behaviour has been previously predicted via modelling or identified ex situ and attributed to oriented attachment [26, 50]

The radiolytic dissolution of ceria is now established as a quantified rate R, within a range around R = 100 $gday^{-1}m^{-2}$ which is exceptionally high compared to any earlier reports. Here our extended results compared to our earlier short report [31], confirm the validity for a variety of shapes and sized of particles (including nanorods), but also for two acceleration voltages (200 and 300 kV).

Hydrogen bubble formation is observed for the first time in a single experiment relative to ceria corrosion. The observed need for significantly higher dose rate for bubble visibility compared to the ceria-dissolution reactions, points to a dominance of direct radiolysis rather than reactive-surface induced H_2 production. This is of relevance to research fields involving the triple-combination of radiation, reactive oxides or alloys, and water, whether in catalysis chemistry [47, 51], or in nuclear engineering [52, 53]

The significance of the overall findings are due to their relevance for a variety of industrial and biomedical applications, e.g. catalytic, environmental, polishing, corrosion, recycling, nuclear fuels and waste disposal, but also cellular radiation protection in radiotherapy. All those fields critically depend on understanding the water-ceria reaction front.

Acknowledgments

Funding contributions for this project have been received by EPSRC, UK (EP/J021199/1), University of Sheffield, UK, and NED University of Engineering and Technology, Karachi, Pakistan.

ORCID iDs

Muhammad Sajid Ali Asghar https://orcid.org/0000-0002-9184-9098
Beverley Inkson https://orcid.org/0000-0002-2631-9090
Sudipta Seal https://orcid.org/0000-0002-0963-3344
Marco Molinari https://orcid.org/0000-0001-7144-6075
Dean Sayle https://orcid.org/0000-0001-7227-9010
Günter Möbus https://orcid.org/0000-0003-4615-1499

References

[1] Gangopadhyay S, Frolov D D, Masunov A E and Seal S 2014 Journal of Alloys and Compounds 584 199
[2] Feng X et al 2006 Science 312 1504
[3] Yabe S and Sato T 2003 Journal of Solid State Chemistry 171 7
[4] Harvey T G 2013 Corrosion Engineering, Science and Technology 48 248
[5] Montini T, Melchionna M, Monai M and Fornasiero P 2016 Chem. Rev. 116 5987
[6] Zhong L-S, Hu J-S, Cao A-M, Liu Q, Song W-G and Wan L-J 2007 Chem. Mater. 19 1648
[7] Trovarelli A, Leitenburg C d, Boaro M and Dolcetti G 1999 Catalysis Today 50 353
[8] Karakoti A S, Monteiro-Riviere N A, Aggarwal R, Davis J P, Narayan R J, Self W T, McGinnis J and Seal S 2008 JOM 60 33
[9] Das M, Patil S, Bhargava N, Kang J F, Riedel L M, Seal S and Hickman J J 2007 Biomaterials 28 1918
[10] Tarnuzzer R W, Colon J, Patil S and Seal S 2005 Nano Letters 5 2573
[11] Ouyang Z, Mainali M K, Sinha N, Strack G, Altundal Y, Hao Y, Winningham T A, Sajo E, Celli J and Ngwa W 2016 Phys Med 32 631
[12] Corkhill C L, Bailey D J, Tocino F Y, Stennett M C, Miller J A, Provis J L, Travis K P and Hyatt N C 2016 Appl. Mater. Interfaces 8 10562
[13] Möbus G, Saghi Z, Sayle D C, Bhatta U M, Stringfellow A and Sayle T X T 2011 Adv. Funct. Mater. 21 1971
[14] Virot M, Chave T, Horlait D, Clavier N, Dacheux N, Ravaux J and Nikitenk S I 2012 J. Mater. Chem. 22 14734
[15] de Jonge N, Poirier-Demers N, Demers H, Peckys D B and Drouin D 2010 Ultramicroscopy 110 1114
[16] de Jonge N and Ross F M 2011 Nature Nanotechnology 6 695
[17] Kraus T and de Jonge N 2013 Langmuir 29 8427
[18] Williamson M J, Tromp R M, Vereecken P M, Hull R and Ross F M 2003 Nature Materials 2 532
[19] WookNoh K, Liu Y, Sun L and Dillon S 2012 Ultramicroscopy 116 34
[20] Jiang Y, Zhu G, Lin F, Zhang H, Jin C, Yuan J, Yang D and Zhang Z 2014 Nano Lett 14 3761
[21] Molinari M, Parker S C, Sayle D C and Islam M S 2012 J. Phys. Chem. C 116 7073
[22] Hansen H A and Wolverton C 2014 J. Phys. Chem. C 118 27402
[23] Zhang C et al 2013 J. Am. Chem. Soc. 135 11572
[24] Juillet F, Adnet J M and Gasgnier M 1997 Journal of Radioanalytical and Nuclear Chemistry 224 137
[25] Popel A J, Solliec S L, Lampronti G I, Day J, Petrov P K and Farnan I 2017 Journal of Nuclear Materials 484 332
[26] Plakhova T V et al 2016 J. Phys. Chem. C 120 22615
[27] Channei D, Phanichphant S, Nakaruk A, Mofarah S S, Koshy P and Sorrell C C 2017 Catalysts 7 1
[28] Karakoti A S, Kuchibhatla S V N T, Babu K S and Seal S 2007 J. Phys. Chem. C 111 17232
[29] Yu P, Hayes S A, O'Keefe T J, O'Keefe M J and Stoffer J O 2006 Journal of The Electrochemical Society 153 C74
[30] Ikeda-Ohno A, Hennig C, Weiss S, Yaita T and Bernhard G 2013 Chem. Eur. J. 19 7348
[31] Asghar M S A, Inkson B and Möbus G 2017 Chem. Phys. Chem. 18 1247
[32] Xu X, Saghi Z, Gay R and Möbus G 2007 Nanotechnology 18 225501
[33] Sakthivel T, Das S, Kumar A, Reid D L, Gupta A, Sayle D C and Seal S 2013 Chem Plus Chem 78 1446–55
[34] Sakthivel T S, Reid D L, Bhatta U M, Möbus G, Sayle D C and Seal S 2015 Nanoscale 7 5169
[35] Klein K L, Anderson I M and de Jonge N 2011 J. Microsc. 242 117
[36] Schneider N M, Norton M M, Mendel B J, Grogan J M, Ross F M and Bau H H 2014 J. Phys. Chem. C 118 22373
[37] Evans J E, Jungjohann K L, Browning N D and Arslan I 2011 Nano Lett 11 2809
[38] Liang W-I, Zhang X, Bustillo K, Chiu C-H, Wu W-W, Xu J, Chu Y-H and Zheng H 2015 Chem. Mater. 27 8146
[39] Nielsen M H, Aloni S and De Yoreo J J 2014 Science 345 1158
[40] Bian S-W, Mudunkotuwa I A, Rupasinghe T and Grassian V H 2011 Langmuir 27 6059
[41] Vincent A, Inerbaev T M, Babu S, Karakoti A S, Self W T, Masunov A E and Seal S 2010 Langmuir 26 7188
[42] Dahle J T, Livi K and Arai Y 2015 Chemosphere 119 1365
[43] Heisbourg G, Hubert S, Dacheux N and Purans J 2004 Journal of Nuclear Materials 335 5
[44] Sayle T X T, Molinari M, Das S, Bhatta U M, Möbus G, Parker S C, Sealc S and Sayle D C 2013 Nanoscale 5 6063
[45] Neck V, Müller R, Bouby M, Altmaier M, Rothe J, Denecke M and Kim J 2002 Radiochim. Acta 90 485
[46] Woehl T J, Jungjohann K L, Evans J E, Arslan I, Ristenpart W D and Browning N D 2013 Ultramicroscopy 127 53
[47] Caër S L 2011 Water 3 235
[48] Abellan P, Moser T H, Lucas I T, Grate J W, Evans J E and Browning N D 2017 RSC Adv. 7 3831
[49] Lu Y, Geng J, Wang K, Zhang W, Ding W, Zheng Z, Xie S, Dai H, Chen F-R and Sui M 2017 ACS Nano 11 8018
[50] Ji Z, Wang X, Zhang H, Lin S, Meng H, Sun B, George S, Xia T, Nel A E and Zink J I 2012 ACS Nano 6 5366
[51] LaVerne J A and Tandon L 2002 J. Phys. Chem. B 106 380
[52] Ewing R C 2015 Nature Materials 14 252
[53] Saji G 2014 ASME Proceedings, 22nd International conference on nuclear engineering 22 (Paper No ICONE22-30991) pp V001T02A026